Nanoparticle proximity controls selectivity in benzaldehyde hydrogenation

Manuscript – article

Nanoparticle proximity controls selectivity in benzaldehyde hydrogenation

Kang Rui Garrick Lim[1,2,4], Selina K. Kaiser[1,2,4], Haichao Wu[2], Sadhya Garg[2], Marta Perxés Perich[3], Jessi E. S. van der Hoeven[3], Michael Aizenberg[2], Joanna Aizenberg[1,2,*]

[1] Department of Chemistry and Chemical Biology, Harvard University, Cambridge, Massachusetts 02138, United States

[2] John A. Paulson School of Engineering and Applied Sciences, Harvard University, Cambridge, Massachusetts 02138, United States

[3] Materials Chemistry and Catalysis, Debye Institute for Nanomaterials Science, Utrecht University, 3584 CG Utrecht, Netherlands

[4] These authors contributed equally to this work

* Corresponding author. Email: jaiz@seas.harvard.edu (J. A.)

ABSTRACT

Disentangling the effects of nanoparticle proximity and size on thermal catalytic performance is challenging with traditional synthetic methods. Here, we adopt a modular raspberry-colloid-templating approach to tune the average interparticle distance, while preserving all other physicochemical characteristics, including nanoparticle size. By controlling the metal loading and placement of pre-formed nanoparticles within a 3D macroporous support and using the hydrogenation of benzaldehyde to benzyl alcohol and toluene as our probe reaction, we report that increasing the interparticle distance (12 to 21 nm) substantially enhances selectivity towards benzyl alcohol (54 to 99%) without compromising catalytic activity or stability. Combining electron tomography, kinetic evaluation, and simulations, we show that interparticle distance modulates the local benzyl alcohol concentration profile between active sites, consequently affecting benzyl alcohol readsorption, which promotes hydrogenolysis to toluene. Our results illustrate the relevance of proximity effects as a mesoscale tool to control the adsorption of intermediates and hence, catalytic performance.

SUBJECTS: catalyst design, proximity effects, colloidal templating, thermal catalysis, hydrogenation, diffusion, adsorption

Heterogeneous catalysis play a central role in the production of more than 90% of chemicals manufactured globally[1] by reducing the energy costs and environmental impact through improved energy efficiency and product selectivity.[2] Supported metal-based catalysts typically consist of nanoparticles (NPs) deposited on solid supports[3] which facilitate mass transport and enhance catalytic performance through dispersion and NP–support interactions.[4] While it is well-known that the NPs (*e.g.*, size, composition, shape),[5,6] support properties (*e.g.*, surface acidity, porosity),[7] and the interactions between them (*e.g.*, metal–support interactions, charge transfer)[4,8] all contribute to the overall catalytic performance, the effect of NP proximity,[9,10] beyond its impact on NP sintering and stability in thermal catalysis,[11–16] is not elucidated. Given that NP proximity has been reported to alter catalytic activity[17–19] and selectivity[20–23] in electrocatalytic (*via* concentration gradients)[17,20–22] and surface science studies (*via* reactant spillover between adjacent NPs across the support),[24] we hypothesize that NP proximity can be used in thermal catalysis to modulate catalytic activity and/or selectivity of supported metal-based catalysts, complementing prior work exploiting pore confinement effects in diffusion-limited micro- and mesoporous materials.[25–28]

However, systematic investigations on NP proximity effects in thermal catalysis are challenging when relying on traditional precipitation or impregnation methods where the metal precursor is introduced to the support, followed by NP nucleation.[3] A higher concentration of the metal precursor increases the metal loading and number of NPs, thereby reducing the interparticle distance, but concomitantly yields larger NPs,[29,30] which does not decouple the direct effects of NP proximity and size on catalysis (**Supplementary Fig. 1a**). An alternative approach involves immobilizing pre-synthesized colloidal NPs, with well-defined NP sizes and stabilized by ligands, onto the support (**Supplementary Fig. 1b**).[31,32] This approach, however, demands careful design and control of the subsequent ligand removal step to expose the metal NP surfaces for catalysis[33,34] while avoiding NP sintering – the most common negative effect that leads to the increase of NP sizes, dislodging, and/or spatial redistribution.[3,35] Deconvoluting NP proximity effects from changes in NP size on catalytic performance thus requires a different catalyst platform capable of independently varying these potential descriptors.[36]

To systematically investigate how NP proximity effects influence thermal catalytic performance, we adapt the raspberry-colloid-templating (RCT) approach [37] to fabricate a series of 3D macroporous PdAu/SiO_2 catalysts whose average interparticle distance was tuned by metal loading at a fixed NP size (**Fig. 1a**). This catalyst platform is used to investigate the effect of interparticle distance on the liquid phase hydrogenation of benzaldehyde (BA) to benzyl alcohol (BOH, desirable product) and toluene (TOL, side product of hydrogenolysis). BA hydrogenation was selected as our model reaction as the initial hydrogenation of BA to BOH proceeds cleanly with high selectivity,[38–40] and its thermal catalytic mechanism[41,42] and kinetic parameters are well established.[43]

We separately study the effect of NP proximity on BA hydrogenation under constant BA conversion kinetics or mass transport conditions. To further decouple the metal loading from interparticle distance, the highly modular RCT method is developed to design locally high-metal-density RCT catalysts (**Fig. 1b**) to investigate the NP proximity effect under both

abovementioned conditions simultaneously. We report that reducing the metal loading increases the average interparticle distance, which, in turn, improves the selectivity towards BOH independent of catalytic activity and stability, thereby circumventing commonly found activity-selectivity trade-offs. Simulations reveal that larger interparticle distances lower the local BOH concentration profile between the NPs during BA conversion to BOH, reducing BOH readsorption to the NPs and minimizing further reaction to TOL (**Fig. 1c–d**). Our experimental and simulation results provide direct evidence that NP proximity effects can play a critical role in tuning the selectivity in thermal catalysis and thus, should be considered in future catalyst design.

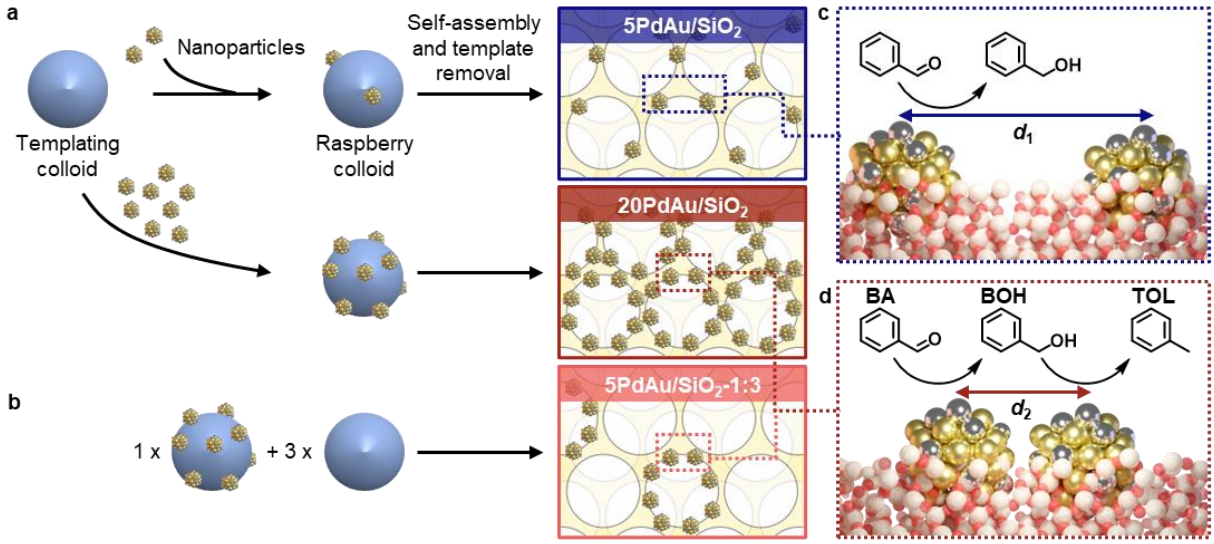

Fig. 1: Synthetic strategy to investigate the effect of NP proximity on BA hydrogenation. (a) The average interparticle distance (d_1, d_2) of RCT catalysts was tuned by varying the metal loading at a preserved NP size. *x*PdAu/SiO_2 refer to $Pd_{12}Au_{88}/SiO_2$ RCT catalysts with an overall metal loading of *x* wt %. (b) The interparticle distance was further decoupled from the metal loading by combining NP-decorated (*i.e.*, 20 wt %) and NP-free templating colloids in the respective ratio (*i.e.*, 1:3) to a desired overall metal loading (*i.e.*, 5 wt %). *x*PdAu/SiO_2-1:*y* refer to locally high-metal-density $Pd_{12}Au_{88}/SiO_2$ RCT catalysts with an overall metal loading of *x* wt % prepared by diluting high-metal-density raspberry colloids with NP-free colloids in a ratio of 1:*y*. Schematics are not drawn to scale and NPs are enlarged relative to the pore size to increase visibility of the NPs. Anticipated effect of a (c) larger or (d) smaller average interparticle distance on BA hydrogenation selectivity. Gold, silver, white, and red spheres represent Au, Pd, Si, and O atoms, respectively.

RESULTS

Tuning interparticle distance at a preserved NP size. The RCT approach was adapted to prepare catalysts with NPs partially embedded in well-defined 3D macroporous SiO_2 structures to confer strong resistance against sintering during catalysis (**Supplementary Fig. 1c, Methods Section**).[37,44] In brief, Au NPs were attached to monodisperse thiol-functionalized polystyrene (PS) templating colloids to form NP-decorated raspberry colloids. Pd overgrowth was then induced on the Au NPs decorating the raspberry colloids. The latter were self-assembled into a 3D colloidal crystal prior to infiltration with a SiO_2 precursor, followed by calcination that yields homogeneously alloyed NPs, removes the organic PS template, and forms the 3D macroporous SiO_2 support. We refer to $Pd_{12}Au_{88}/SiO_2$ RCT catalysts with an overall metal loading of *x* wt % as *x*PdAu/SiO_2, where *x* = 5, 10, 15, or 20.

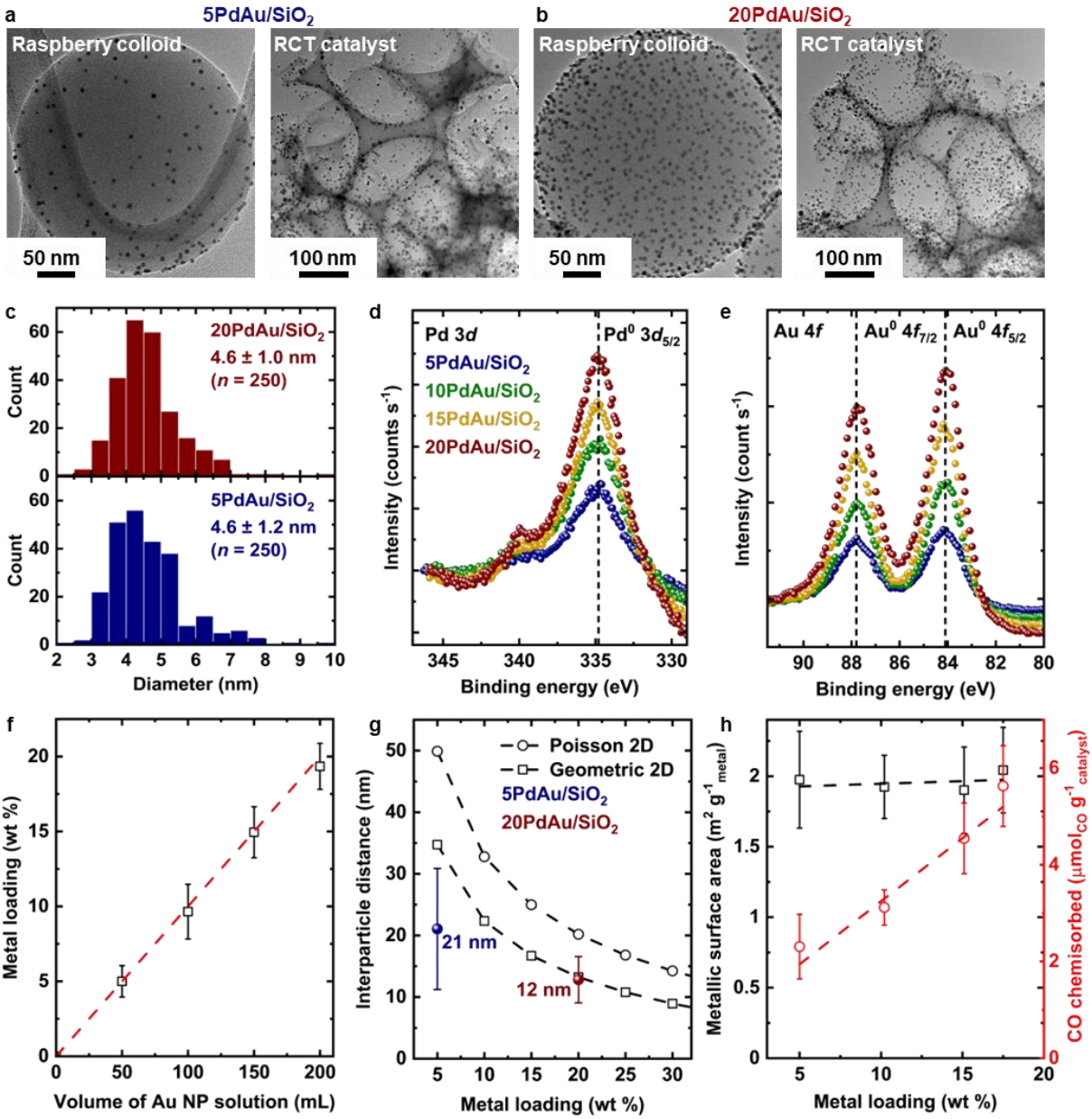

Fig. 2: Physical characterization of RCT catalysts. BF-TEM images depicting raspberry colloids and their resulting RCT catalysts for (a) 5PdAu/SiO_2 and (b) 20PdAu/SiO_2. (c) NP size distribution of RCT catalysts. XPS spectra of RCT catalysts: (d) Pd 3*d* and (e) Au 4*f*. (f) ICP-MS analysis of RCT catalysts. Data presented as mean values with error bars representing the standard deviation of three independent synthetic replicates for each catalyst (n = 3). (g) Interparticle distance of RCT catalysts at different metal loadings as determined by electron tomography (filled circles) and predicted using a 2D geometric (open squares) or statistical Poisson (open circles) model. Interparticle distance data determined by tomography is presented as mean values with error bars representing the standard deviation of n = 657 and n = 2036 measurements from 5PdAu/SiO_2 and 20PdAu/SiO_2, respectively. (h) Metallic surface area (open squares, normalized by mass of metal NPs) and quantity of CO chemisorbed (open circles, normalized by mass of catalyst) by the RCT catalysts at various metal loadings, as determined by volumetric CO chemisorption. Data presented as mean values with error bars representing the standard deviation of three repeat measurements for each catalyst (n = 3). Dotted lines in (d)–(h) are guides to the eye.

Bright field transmission electron microscopy (BF-TEM) and scanning transmission electron microscopy-energy dispersive X-ray spectroscopy (STEM-EDX) depict

homogeneously alloyed PdAu NPs with a uniform size distribution (4.6 ± 1.2 nm) without NP aggregation (**Fig. 2a–c, Supplementary Fig. 2**). The metal loading increases linearly with the volume of NP solution added, evident from the inductively coupled plasma-mass spectrometry (ICP-MS) and X-ray photoelectron spectroscopy (XPS) peak height data (**Fig. 2d–f, Supplementary Table 1**). This finding corroborates with the increasing NP density observed on both the raspberry colloids and resultant RCT catalysts (**Fig. 2a–b, Supplementary Fig. 2a–c**), suggesting strong NP attachment to templating colloids (**Supplementary Fig. 3**). A higher metal loading consequently resulted in shorter interparticle distances, which was confirmed experimentally using electron tomography to determine the 3D coordinates of NPs (d = 21 and 12 nm in 5PdAu/SiO_2 and 20PdAu/SiO_2, respectively; **Fig. 2g, Supplementary Fig. 4, Supplementary Video 1–4, Supplementary Note 1**),[44,45] in agreement with geometric and statistical modeling predictions of interparticle distances (**Fig. 2g, Supplementary Note 2**).[46,47]

While the interparticle distance was varied by metal loading, the NP composition and oxidation states were preserved, evident from ICP-MS values and XPS peak position analyses (**Supplementary Table 1, Supplementary Fig. 6**), respectively. This conclusion was further substantiated by the linear relationship between the quantity of CO chemisorbed and the metal loading (**Fig. 2h, Supplementary Note 3**), indicating that Pd active site accessibility scales linearly and was unrestricted in the investigated range of metal loadings. In conclusion, no apparent physical and chemical differences were detectable apart from the controlled metal loading and hence, average interparticle distance, across the RCT catalyst platform.

To decouple the metal loading from interparticle distance, we devised the self-assembly step to combine high-metal-density raspberry colloids (used in the synthesis of 10/15/20PdAu/SiO_2) with NP-free, bare PS templating colloids as a diluent during the self-assembly process (**Fig. 1b, Supplementary Fig. 7**). Following this strategy, the interparticle distance was controlled by the NP density on the raspberry colloids used, while the overall metal loading can be fixed at any arbitrary value (*e.g.,* 5 wt % in **Fig. 1b**) by mixing the raspberry and NP-free PS colloids in an appropriate ratio. These locally high-metal-density RCT catalysts are referred to as 5PdAu/SiO_2-1:y, where 1:y represents the volume dilution ratio used to obtain an overall metal loading of 5 wt % for direct comparison to 5PdAu/SiO_2 (with similar metal loading), and to 10/15/20PdAu/SiO_2 (with similar interparticle distances when y = 1, 2, or 3, respectively).

Interparticle distance controls catalytic selectivity. Liquid phase BA hydrogenation was performed over 3–15 mg of sieved RCT catalysts loaded into a stainless steel batch reactor at 150 °C and 20 bar H_2 for 24 h, using 50 mM BA in isopropanol, as guided by previous work.[48] Sample aliquots were withdrawn at fixed time intervals and analyzed by *ex situ* gas chromatography-mass spectrometry (GC-MS) using o-xylene as an internal standard.[40] We first investigated the NP proximity effect on BA hydrogenation using constant metal (**Fig. 3a (1)**, m_{metal}) or catalyst mass (**Fig. 3a (2)**, m_{cat}), which afforded the conditions of similar BA conversion kinetics or bulk mass transfer characteristics, respectively. To account for the possibility of BA conversion kinetics affecting mass transport and *vice versa*, locally high-metal-density RCT catalysts were compared against 5PdAu/SiO_2 using both constant metal and

catalyst mass (**Fig. 3a (3)**) to directly investigate NP proximity effects under both abovementioned conditions simultaneously. The results are summarized in **Table 1**. For clarity, only results from the first 12 h of reaction using RCT catalysts at the two extreme interparticle distances are shown in **Fig. 3b–i**, while the complete data range including the whole RCT catalyst series is provided in **Supplementary Fig. 8b–i**. No differences were observed in the BA catalytic parameters (reaction orders and apparent activation energy) between RCT catalysts with different metal loadings (**Supplementary Fig. 9a–c**), and in the physical and chemical characteristics (NP composition, size, and oxidation states) between the fresh and used catalysts (**Supplementary Fig. 9d–i**).

Table 1: Summary of catalytic data.

Catalyst	m_{cat} (mg)	m_{metal} (mg)	t for X(BA) = 100% (h)	S(BOH) at X(BA) = 100% (%)*	S(BOH) at t = 11 h (%)*	k (h^{-1})
(1) Constant metal mass ($m_{metal,1} = m_{metal,2}$)						
$5Au/SiO_2$	12.5	0.6	> 24	N.A.†	N.A.†	< 0.01
$5PdAu/SiO_2$‡ (d = 21 nm)	12.0	0.6	5	99.2 ± 0.2	99.1 ± 0.2	1.0
$10PdAu/SiO_2$	5.9	0.6	6	98.6 ± 0.7	98.5 ± 1.0	1.1
$15PdAu/SiO_2$	3.9	0.6	5	96.8 ± 0.4	96.6 ± 1.7	1.0
$20PdAu/SiO_2$ (d = 12 nm)	3.1	0.6	5	91.4 ± 2.5	91.0 ± 2.0	1.1
(2) Constant catalyst mass ($m_{cat,1} = m_{cat,2}$)						
$5PdAu/SiO_2$‡ (d = 21 nm)	12.0	0.6	5	99.2 ± 0.2	99.1 ± 0.2	1.0
$10PdAu/SiO_2$	12.2	1.2	1	95.9 ± 0.5	94.6 ± 0.2	4.1
$15PdAu/SiO_2$	12.1	1.8	1	79.1 ± 3.0	71.2 ± 3.3	5.7
$20PdAu/SiO_2$ (d = 12 nm)	12.1	2.4	0.75	73.6 ± 2.8	54.4 ± 3.1	8.6
(3) Constant metal and catalyst mass ($m_{metal,1} = m_{metal,2}$ and $m_{cat,1} = m_{cat,2}$)						
$5PdAu/SiO_2$‡ (d = 21 nm)	12.0	0.6	5	99.2 ± 0.2	99.1 ± 0.2	1.0
$5PdAu/SiO_2$-1:1[a]	12.2	0.6	5	98.7 ± 2.6	98.4 ± 0.2	1.1
$5PdAu/SiO_2$-1:2[b]	12.1	0.6	6	98.7 ± 0.2	98.4 ± 2.8	1.0
$5PdAu/SiO_2$-1:3[c] (d = 12 nm)	12.0	0.6	5	92.4 ± 0.3	91.7 ± 2.8	1.0

k, d, m_{cat}, and m_{metal} refer to the first order BA hydrogenation rate constant, average interparticle distance of the catalyst, catalyst mass used, and metal mass used, respectively. $m_{metal} = m_{cat}$ × metal loading in the RCT catalyst. *Standard deviation of three independent synthetic replicates is provided for S(BOH) of each catalyst (n = 3). †S(BOH) for Au/SiO_2 not provided due to their notably lower BA hydrogenation activity. ‡Repeated entry for comparison. [a]5 wt % RCT catalyst formed by assembling 10 wt % raspberry colloids with NP-free colloids in a 1:1 ratio. [b]5 wt % RCT catalyst formed by assembling 15 wt % raspberry colloids with NP-free colloids in a 1:2 ratio. [c]5 wt % RCT catalyst formed by assembling 20 wt % raspberry colloids with NP-free colloids in a 1:3 ratio.

The RCT catalysts were tested using constant metal mass (first set of rows in **Table 1**) to determine if BA hydrogenation activity and/or selectivity was affected by metal loading and hence, interparticle distance. A constant m_{metal} of 0.6 mg was maintained by adjusting m_{cat} to account for the different metal loading amongst the RCT catalysts. $5Au/SiO_2$ (without Pd) was practically inactive for BA hydrogenation under the applied conditions (**Supplementary Fig.**

8b), implying that Pd served as the active sites in the PdAu/SiO_2 catalysts. Following previous literature, we used SiO_2 as a catalytically inert non-reducible support to eliminate NP–support interactions,[49] and bimetallic PdAu NPs to combine the high activity and selectivity of Pd and Au, respectively.[40,50]

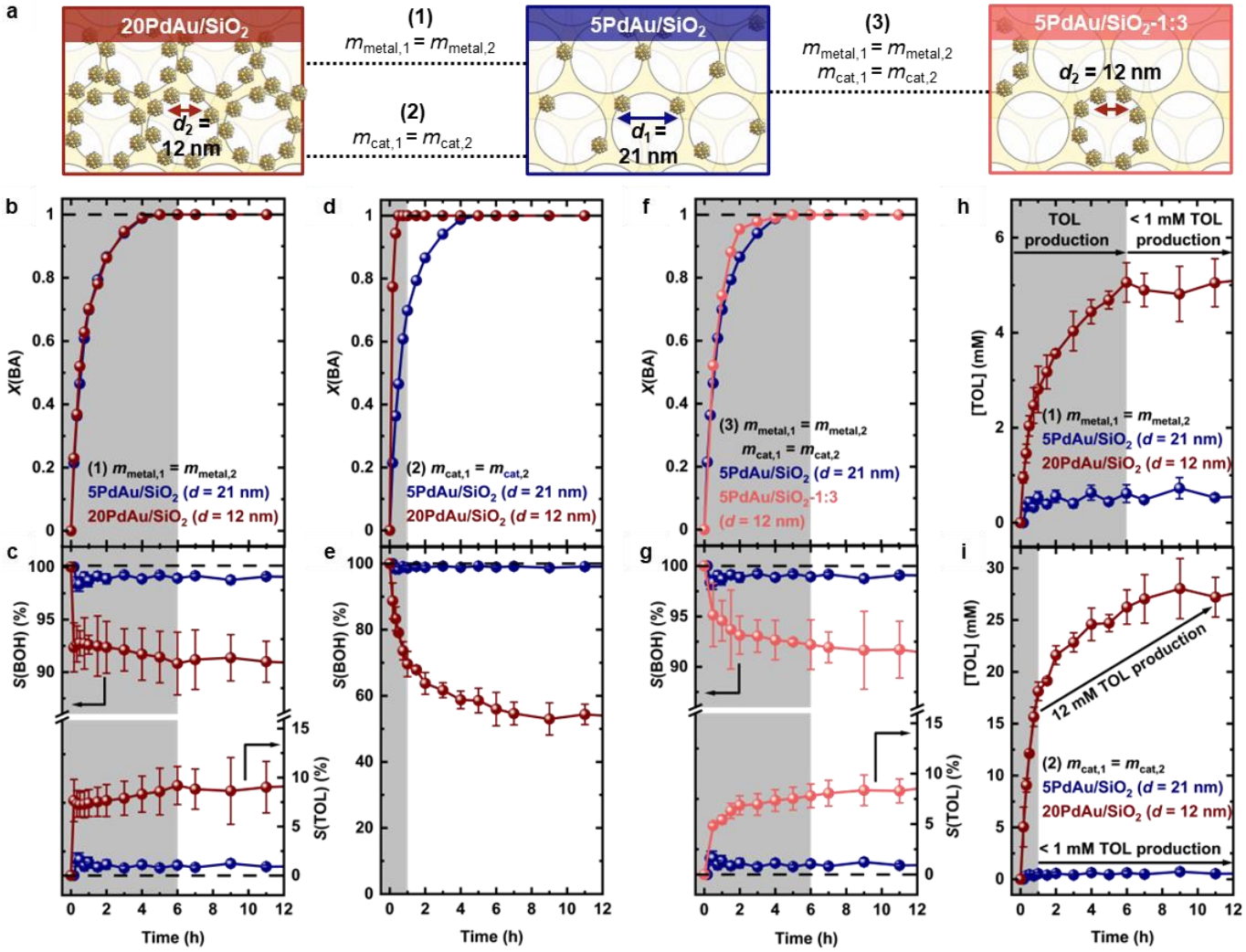

Fig. 3: Liquid phase BA hydrogenation over RCT catalysts. (a) The effect of NP proximity on BA hydrogenation was systematically investigated using constant (1) metal (m_{metal}) or (2) catalyst mass (m_{cat}), which ensures similar (1) BA conversion or (2) bulk mass transfer characteristics, respectively. (3) Locally high-metal-density RCT catalysts with a metal loading of 5 wt % and interparticle distance d = 12 nm were compared to 5PdAu/SiO_2 with interparticle distance d = 21 nm, using both constant metal and catalyst mass to account for BA conversion kinetics affecting mass transport and *vice versa*. (b) BA conversion, (c) selectivity to BOH and TOL, and (h) TOL production as a function of reaction time, using constant metal mass. (d) BA conversion, (e) selectivity to BOH, and (i) TOL production as a function of reaction time, using constant catalyst mass. (f) BA conversion and (g) selectivity of BOH and TOL as a function of reaction time, using locally high-metal-density RCT catalysts at both constant metal and catalyst mass. In all plots, reaction time before and after full BA conversion is indicated by the shaded and unshaded regions, respectively. In (b)–(i), one experimental data set is shown for each curve in each plot. Error bars for (c), (e), (g), (h), and (i) represent the standard deviation of three independent synthetic replicates for each catalyst (n = 3). Full plots with data from other RCT catalysts at intermediate metal loadings are provided in **Supplementary Fig. 8b–i**.

The rate of BA conversion, X(BA), was similar regardless of the metal loading, and hence, interparticle distance, achieving full BA conversion in 6 h (**Fig. 3b, Supplementary Fig. 8b**) with comparable first order rate constants (k, **Table 1**). We reason that the similar BA conversion rates were due to the fixed m_{metal} and therefore, the reactant : Pd active site ratio (≈ 4300), and the unchanged NP composition, size, and oxidation states after catalysis (**Supplementary Fig. 9d–i**). This result implies that both catalytic activity and stability were unaffected by NP proximity, with the stability directly attributed to the partial NP embedding within the RCT support matrix that conferred strong resistance against sintering.[40,44]

Unlike catalytic activity and stability that were both unaffected by NP proximity, BOH selectivity, S(BOH), exhibited a clear dependence on interparticle distance (**Fig. 3c, Supplementary Fig. 8c**). Notably, NP proximity-induced differences in S(BOH) between 5PdAu/SiO_2 and 20PdAu/SiO_2 can be substantially augmented from (99 to 91%) to (97 to 54%) under specific reaction conditions, as exemplified by catalytic tests whereby the reactant : Pd ratio was reduced from 4300 to 1100 (**Supplementary Note 4, Supplementary Fig. 10, Supplementary Table 3**). In line with earlier reports, the primary product of BA hydrogenation was BOH (**Fig. 3c, Supplementary Fig. 8c**, > 90% selectivity)[38] with TOL as an undesired by-product from hydrogenolysis,[40,43,51] at a mass balance error below 5% (**Supplementary Fig. 8a**). No aromatic ring hydrogenation was detected under the reaction conditions used, similar to previous work.[40,41]

To eliminate variations in external bulk mass transport arising from differences in m_{cat} used, we tested RCT catalysts using a fixed catalyst mass (m_{cat} = 12 mg, second set of rows in **Table 1**). As expected, k increased linearly with metal loading (**Supplementary Fig. 8j**) as the number of active sites scales linearly with metal loading at a fixed m_{cat}: full BA conversion was achieved in 1 h for 20PdAu/SiO_2, compared to 5–6 h for 5PdAu/SiO_2 (**Fig. 3d, Supplementary Fig. 8d**). Using fixed m_{cat}, the effect of NP proximity on S(BOH) was even more pronounced: 5PdAu/SiO_2 maintains 99% selectivity throughout the reaction but S(BOH) for 20PdAu/SiO_2 was 74% at full BA conversion (t = 1 h), further decreasing to 54% at t = 11 h (**Fig. 3e, Supplementary Fig. 8e**). When normalized by Pd mass, the BOH yield, Y(BOH), was three times higher for 5PdAu/SiO_2 than for 20PdAu/SiO_2 at t = 1 h, and almost one order of magnitude higher at t = 11 h (**Supplementary Fig. 8k**).

Given that differences in BA conversion kinetics may affect bulk mass transport and *vice versa*, we maintained both conditions simultaneously by comparing locally high-metal-density RCT catalysts against 5PdAu/SiO_2 to verify our findings. The catalysts were compared at fixed metal and catalyst mass, and metal loading (m_{metal} = 0.6 mg, m_{cat} = 12 mg, 5 wt % metal loading, third set of rows in **Table 1**), varying only the interparticle distance. Indeed, BA catalytic activity was comparable in all locally high-metal-density catalysts regardless of interparticle distance (**Fig. 3f, Supplementary Fig. 8f**), whereas catalysts prepared using raspberry colloids with the highest NP density and hence, shortest interparticle distances, displayed the lowest S(BOH) (**Fig. 3g, Supplementary Fig. 8g**). Taken together, the catalytic results illustrate that the interparticle distance can be tailored to independently control catalytic selectivity without compromising catalytic activity (**Fig. 3b–e, Supplementary Fig. 8b–e**) and

stability, even when catalysts of the same metal loading, metal mass, and catalyst mass are compared (**Fig. 3g, Supplementary Fig. 8g**).

Kinetic analysis of BA hydrogenation. To determine if TOL was produced in a concerted (direct BA hydrogenolysis to TOL) and/or stepwise manner (TOL from hydrogenolysis of BOH *via* BA) under the applied reaction conditions, kinetic analyses were performed. Tracking the concentration of TOL, [TOL], during the reaction reveals that TOL production primarily occurred during, as compared to after, full BA conversion (shaded regions in **Fig. 3h–i, Supplementary Fig. 8h–i**). Moreover, the quantity of TOL produced was highly dependent on the interparticle distance in the RCT catalysts, reflecting the effects of NP proximity on *S*(BOH) and, consequently, on [TOL]. The first observation was initially unexpected as the BOH concentration, [BOH], was much lower during BA conversion since BOH was being actively produced (**Supplementary Fig. 8k**). Furthermore, both observations persisted even as the reaction was left to run for 24 h (**Supplementary Fig. 8h**), suggesting that the rate of BOH conversion to TOL was much slower than that of BA to BOH. When m_{cat} was fixed, TOL formation continued after full BA conversion (t > 1 h) for the 15PdAu/SiO_2 and 20PdAu/SiO_2 RCT catalysts (**Fig. 3i, Supplementary Fig. 8i**), albeit at a substantially slower rate than during BA conversion (t < 1 h), in agreement with the first observation. We reason that the slow, but non-negligible, TOL formation in the high-metal-loading RCT catalysts after full BA conversion could be due to the abundance of NPs and hence, Pd active sites, for freely diffusing BOH to adsorb onto for conversion to TOL.

To gain further insights into the kinetics of BOH conversion to TOL, we conducted a control reaction under similar conditions but using 50 mM BOH, instead of 50 mM BA, as the reactant. Only 8% and 20% BOH conversion (to TOL) was recorded after 11 h under fixed m_{metal} and m_{cat} conditions, respectively (**Supplementary Fig. 11**), confirming that BOH to TOL conversion was indeed much slower than BA to BOH conversion. A close examination of **Supplementary Fig. 11** depicts 11 mM of TOL produced after 11 h of reaction starting with 50 mM BOH and 12 mg of 20PdAu/SiO_2 catalyst (here, TOL was formed *via* the adsorption of freely diffusing BOH in the bulk liquid onto the NPs). Remarkably, this result parallels the 12 mM of TOL produced in the immediate 10 h after full BA conversion using the same catalyst (unshaded region of t = 1–11 h in **Fig. 3i**, reaction starts with the typical 50 mM BA instead). We thus ascribe the 12 mM of TOL produced after full BA conversion primarily to slow and passive molecular diffusion[52] of BOH from the bulk liquid to the NP for conversion to TOL, following our analysis of **Supplementary Fig. 11**.

To rationalize the differences in catalytic selectivity and TOL production amongst the different catalysts during BA production, we modeled each reaction (BA to BOH, BOH to TOL, BA to TOL) as an elementary Langmuir-Hinshelwood surface reaction to determine their individual contributions to the overall mechanism (**Supplementary Note 5, Supplementary Fig. 12, Supplementary Table 4**).[43] Our kinetic modeling revealed that direct BA hydrogenolysis to TOL (bypassing BOH) was at least two orders of magnitude slower than BA hydrogenation to BOH. Thus, the much slower direct BA hydrogenolysis to TOL cannot be the primary explanation for the high TOL production, and we considered the majority of TOL to be formed from BOH, in agreement with previous experimental kinetic modeling.[43]

Our model suggested that the rate of BOH conversion to TOL depended on factors *intrinsic* to the active site, such as the apparent activation energy (which affects the rate constant k_2) and BOH adsorption coefficient (K_{BOH}), and *external* factors beyond the active site, such as mass transport (γ), and the local concentration of BOH ([BOH]) and active sites ([*]).[43] We thus sought to determine which factor(s) varied between the different catalysts by systematically investigating each factor individually while keeping the others fixed. As there were no observable changes to the reaction parameters or NP physicochemical characteristics post-catalysis (**Supplementary Fig. 9**), *intrinsic* factors (rate constant and BOH adsorption coefficient) should be comparable between the RCT catalysts and not responsible for the observed differences in TOL production and selectivity. The selectivity differences also persisted and were statistically significant ($p < 0.05$, **Supplementary Table 5**) when the catalysts were tested using constant m_{metal} and m_{cat}, both separately and simultaneously (**Fig. 3b–g, Supplementary Fig. 8b–g**), conclusively eliminating variations in both *external* bulk mass transport (*via* constant m_{cat} tests) and BA conversion kinetics (*i.e.,* active site concentration, *via* constant m_{metal} tests) as reasonable causes. Ruling out all these factors led us to deduce that differences in the local BOH concentration profile amongst the RCT catalysts, caused by the different interparticle distances, was the most plausible explanation.

We thus investigated if changes in the local [BOH] could explain the high, rapid, and NP proximity-dependent TOL production during BA conversion, and if so, how interparticle distance influences the local [BOH]. Since the NPs actively produce BOH during BA conversion, we posit that NP proximity plays a pivotal role in augmenting the local [BOH] profile around the NPs.[21] This would consequently affect transient BOH diffusion and readsorption onto the NPs for TOL formation. Similar phenomena were proposed in heterogeneous electrocatalysis,[17,20–22] but remain undocumented in thermal catalysis, possibly due to the high propensity for NP sintering in conventionally prepared catalysts under typical reaction conditions.[12,16]

Elucidating the effect of NP proximity on selectivity. To evaluate how NP proximity affects the local [BOH] profile and subsequently, selectivity, we used the interparticle distance data (**Fig. 2g**) and simulated the local [BOH] profile around the NPs based on a model comprising two NPs on a flat surface (**Supplementary Fig. 13a**). Specifically, the local [BOH] around the NPs at a small (12 nm) and large (21 nm) interparticle distance was simulated using COMSOL to model the 20PdAu/SiO_2 and 5PdAu/SiO_2 RCT catalysts in **Fig. 4a–b**, respectively (details in **Methods section**).[21,22] The simulated [BOH] profile at other interparticle distances are provided in **Supplementary Fig. 13b**. The COMSOL simulations reflect the steady state [BOH] profile around the NPs due to BOH generation by the NPs, and the bulk liquid acting as a BOH sink. We focused on the local [BOH] at the midpoint in between the NPs (**Supplementary Fig. 13a**) as BOH molecules in the immediate vicinity of the NPs are mostly likely to adsorb onto the active sites of those NPs to form TOL. We additionally note that the catalyst's macropore size (300 nm) was more than two orders of magnitude larger than the molecular size of BOH (0.62 nm),[53] and hence, any pore confinement effects on the local [BOH] profile around the NPs were negligible, which was confirmed experimentally (**Supplementary Note 6, Supplementary Fig. 14**).

The trend of local [BOH] at the midpoint as a function of interparticle distance is shown in **Fig. 4c**. As the local [BOH] at the midpoint of the 5PdAu/SiO_2 model is 45% lower than that in the 20PdAu/SiO_2 model, the likelihood of BOH readsorption on the 5PdAu/SiO_2 RCT catalyst is greatly reduced, thereby minimizing TOL production and increasing BOH yield. This conclusion agrees with the experimental data (filled circles in **Fig. 4d**) which indicate a substantial enhancement in *S*(BOH) at t = 11 h from 54 to 99% as the average interparticle distance increases from 12 nm (20PdAu/SiO_2) to 21 nm (5PdAu/SiO_2). We further note that the *S*(BOH) trend at the different interparticle distances (**Fig. 4d**) depict an inverse relationship to the local [BOH] trend (**Fig. 4c**), underscoring the strong correlation between NP proximity and product selectivity.

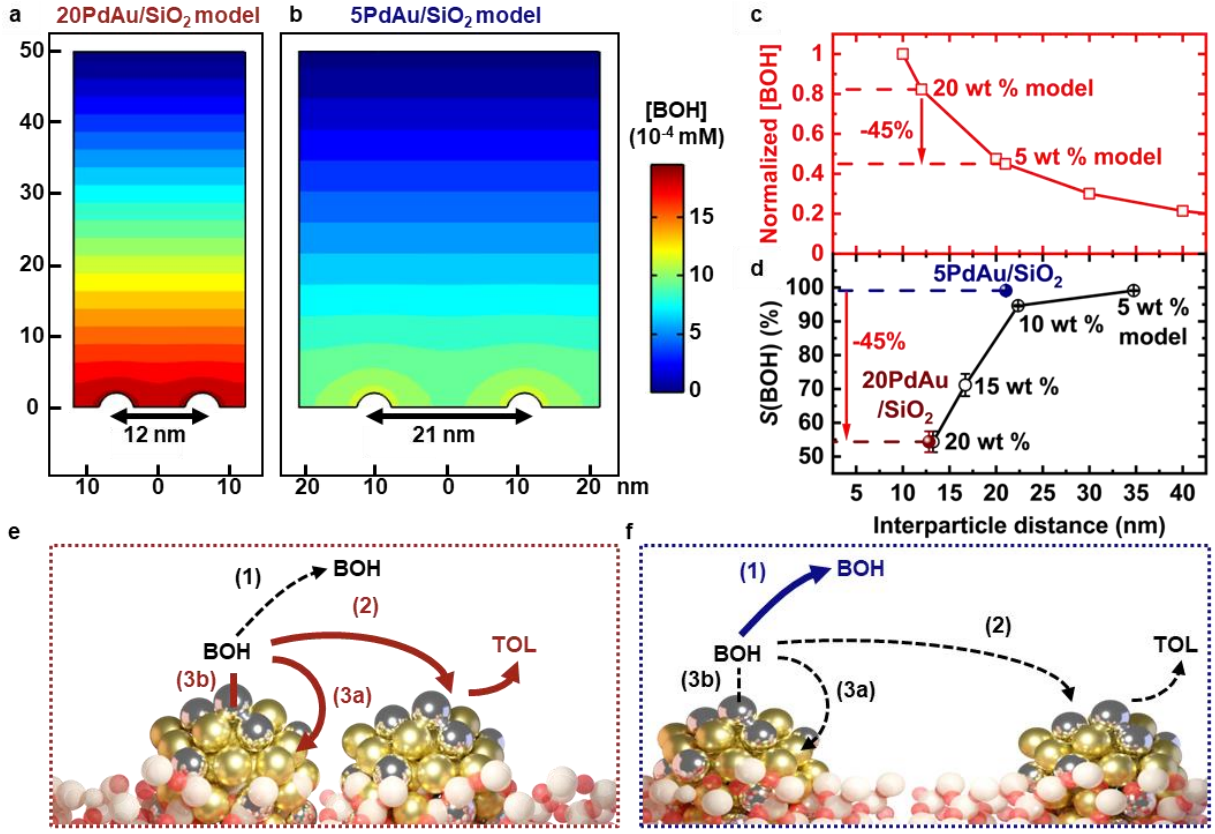

Fig. 4: Effect of NP proximity on local BOH concentration profile. Simulated steady state BOH concentration profile around two NPs during BA conversion at a (a) small (d_2 = 12 nm) and (b) large (d_1 = 21 nm) interparticle distance, modeled after the 20PdAu/SiO_2 and 5PdAu/SiO_2 RCT catalysts, respectively. (c) Normalized [BOH] at the midpoint of the two NPs in the COMSOL simulation at various interparticle distances. (d) BOH selectivity after 11 h using a fixed catalyst mass (m_{cat} = 12 mg) at various interparticle distances either measured by electron tomography (filled circles) or predicted using a geometric 2D model (open circles). Error bars represent the standard deviation in BOH selectivity from three independent synthetic replicates for each catalyst (n = 3). Proposed effect of interparticle distance on BA catalytic selectivity. (e) At small interparticle distances, BOH readsorption is enhanced by the increased local BOH concentration profile around NPs, favoring paths 2, 3a, and 3b, and forming more TOL. (f) At larger interparticle distances, BOH readsorption is diminished due to the depleted local BOH concentration profile around NPs, instead favoring BOH desorption into the bulk (path 1) and thus, forming less TOL. In (e) and (f), bold and dashed arrows indicate the proposed major and minor pathways for BOH, respectively. Gold, silver, white, and red spheres represent Au, Pd, Si, and O atoms, respectively.

Given that the different local [BOH] across the catalysts may affect BA adsorption kinetics, we tracked the BA concentration in a modified reaction using the same starting

reactant (50 mM BA) but spiked with 100 mM BOH to simulate a higher local [BOH] found in the higher metal loading catalysts (**Supplementary Fig. 15**). BA conversion was unaffected by the presence of BOH, demonstrating that any competitive adsorption of BOH has minimal effect on BA adsorption, conversion and hence, BOH production.[42] As a further proof of concept, we tested the 5PdAu/SiO_2 and 10PdAu/SiO_2 catalysts with a three-fold higher starting BA concentration (150 mM). Since the reaction is first order with respect to the starting BA concentration (**Supplementary Fig. 9a**), this test simulates a three-fold higher local [BOH] found in the 20PdAu/SiO_2 catalyst. Indeed, the 10PdAu/SiO_2 catalyst with a three-fold higher starting BA concentration produced TOL at similar rates and quantities as the 20PdAu/SiO_2 catalyst tested at the original BA concentration (**Supplementary Fig. 16**). We thus conclude that NP proximity affects *S*(BOH), which was observed experimentally, *via* altering the local [BOH] around the NPs and affecting BOH readsorption for subsequent reaction to TOL, as revealed by the COMSOL simulations.

We argue that at the molecular level, following hydrogenation of BA to BOH (see the paths depicted in **Fig. 4e–4f**), the as-produced BOH molecule adsorbed on the NP can desorb either into the bulk solution as free BOH (path 1), or stay within the NP's proximity. For the latter, the BOH molecule can desorb from the NP and be rapidly readsorbed by an adjacent NP (path 2) or the same NP (path 3a), without diffusing into the bulk in both cases. Paths 2 and 3a yield TOL and depend on the interparticle distance as a higher local [BOH] would increase effective BOH readsorption to form TOL. Alternatively, the BOH molecule can remain adsorbed on the same NP and form TOL (path 3b). Since the lifetime of BOH adsorbed on a NP depends on the BOH surface coverage on the active sites of the NP, we propose that paths 1 and 3b likewise depend on interparticle distance. Thus, we put forward that interparticle distance affects selectivity and hence, TOL production, *via* two competing routes. Path 1 results in freely diffusing BOH in the bulk, while paths 2, 3a, and 3b produce TOL *via* BOH readsorption to an adjacent NP, or on the same NP, respectively.

Our findings are summarized as follows. First, TOL production is higher and faster during BA conversion than after full BA conversion (**Fig. 3h–i**) as the BOH source differs in both instances. BOH is actively produced by the NP active sites during BA conversion, which raises the local [BOH] profile around NPs for enhanced BOH readsorption to form TOL. After full BA conversion, NPs cease BOH production and BOH is primarily sourced from the slow and passive molecular diffusion of BOH from the bulk solution to the NP.[52] Second, TOL production during BA conversion is affected by the interparticle distance which augments the local [BOH] in between the NPs, affecting BOH readsorption. At larger interparticle distances, a greater fraction of as-produced BOH that desorbs from the NP diffuses into the bulk liquid as free BOH (path 1), as opposed to readsorbing to an adjacent NP (or to the same NP) to form TOL (paths 2 and 3). This is due to the diminished local [BOH] profile between the NPs (**Fig. 4a–c**) with increasing interparticle distance, resulting in enhanced *S*(BOH) (**Fig. 3c, 3e, 3g, 4d**) and hence, reduction in undesired TOL produced (**Fig. 3h–i**).

DISCUSSION

With the RCT method, existing constraints in traditional preparative methods of supported metal-based catalysts can be overcome, enabling a systematic variation of the

interparticle distance at preserved physicochemical parameters, including NP size and metal loading, as verified by a combination of characterization techniques, including electron tomography (**Fig. 2**). The RCT platform also presents a practical and scalable means[54,55] to prepare exceptionally thermally and mechanically stable catalysts with controlled metal loadings, due to the RCT method's unique characteristic to endow stable structures featuring partial embedding of NPs within the support matrix, thus resisting NP dislodging, relocation, and ultimately sintering (*via* Ostwald ripening and/or coalescence), commonly observed in traditional catalysts.[44] With an emerging research interest in high metal loading catalysts,[56,57] we illustrate the utility of the modular RCT method as a well-defined model catalyst platform to systematically interrogate fundamental catalytic descriptors, their combined or individual effects, to bridge the knowledge gaps between surface science and applied catalysis.

Using PdAu/SiO_2 RCT catalysts as an example, we show that catalysts with larger average interparticle distances (21 *vs* 12 nm) exhibit enhanced selectivity in the hydrogenation of BA to BOH (99 *vs* 54%), due to the suppression of further reaction to TOL. Ruling out changes in the kinetics and thermodynamic reaction parameters, as well as the catalyst structure throughout the reaction, the results presented herein clearly demonstrate that NP proximity controls selectivity independent of stability and activity (**Fig. 3b–e**), thus breaking archetypical activity-selectivity tradeoffs. Importantly, by diluting high-metal-density NP-decorated templating colloids with NP-free colloids in the ratio that brings the overall metal loading to a desired and reduced value, while keeping the interparticle distance small (**Fig. 1b**), the selectivity control exerted by NP proximity was further decoupled from metal loading, metal mass, and catalyst mass (**Fig. 3f–g**).

Combining kinetic analysis and computational simulations identifies a correlation between NP proximity and the local BOH concentration profile at the NPs during BA conversion that affects BOH readsorption and hence, subsequent reaction to TOL (**Fig. 4**). The NP proximity effects were identified in a non-confined molecular diffusion regime, different from pore confinement effects reported in micro- and mesoporous materials under confined Knudsen diffusion regimes (**Supplementary Note 6, Supplementary Fig. 14**).[25–28] The NP proximity effects thus also apply to NPs dispersed on non-porous supports in open environments (**Supplementary Note 7, Supplementary Fig. 17**), and in macroporous catalysts (> 50 nm, *e.g.*, support monoliths in automobile exhaust control[58]), since internal diffusion is similarly non-confined in those material architectures. Given that such effects on selectivity can be substantially enhanced under specific reaction conditions (**Supplementary Note 4**), we stress that future work comparing catalysts with different metal loadings should take into account interparticle distances, even when the catalysts are evaluated at the same metal masses and NP size distributions.

This proof-of-concept work that uses the hydrogenation of BA to BOH and TOL as a probe reaction provides direct evidence that NP proximity controls selectivity in thermal catalysis through modulating the local concentrations of intermediates. We note that the interparticle distance can be tuned using a variety of synthetic approaches (*e.g.,* metal loading or controlled NP placement as illustrated in **Fig. 1**, metal dispersion, catalyst dilution, and more) beyond those described in this work to achieve similar effects of NP proximity on

catalytic selectivity. We anticipate that the magnitude of this effect in various reactions will depend on the combinatorial choice of reaction, reaction conditions, and catalyst used, thereby opening opportunities to introduce NP proximity, a physical descriptor present in practically all NP-supported catalysts, into rational catalyst design to direct catalytic performance for specific applications in other heterogeneous catalytic systems.

In particular, we highlight that our results are highly relevant for the emerging application of one-pot tandem reactions and multi-step catalytic cascades,[59,60] whereby the control of the timing and quantity of intermediate(s) produced and/or consumed is of paramount importance, yet difficult to practically control.[61–63] With the high prevalence of supported metal-based catalysts in many catalytic cascade reactions involving multiple steps,[1] these NP proximity effects may be present, compounded in a positive feedback loop, and potentially synergetic, necessitating further kinetic studies to exploit these effects to regulate and achieve non-equilibrium local intermediate concentrations, thus enhancing catalytic selectivity for a broad range of reactions,[62,64] without compromising catalytic activity and/or stability. We further foresee that NP proximity effects may be applicable to multi-functional catalyst architectures with spatially separated active sites, as demonstrated here for the locally high-metal-density RCT catalysts (**Fig. 1b**). Similarly, the deliberate concentration of metallic NPs in local areas of zeolites[65,66] and hierarchically porous structures[61,67] will not only reduce the overall metal loading, but also induce or augment NP proximity effects in these specific regions of the catalyst. Our results suggest that employing interparticle distances as a mesoscale tool, either independently or in concert with other known tools, both intrinsic (*e.g.*, NP size and composition, support chemistry)[5,6] and extrinsic (*e.g.*, reactor design and engineering controls), may potentially exert even greater control over catalytic selectivity.

METHODS

Chemicals. All chemicals were used as received without further purification. Tetrachloroauric (III) acid trihydrate ($HAuCl_4 \cdot 3H_2O$, ≥99.9% trace metal basis), sodium tetrachloropalladate (II) (Na_2PdCl_4, 98%), sodium citrate tribasic dihydrate (≥99.0%), potassium carbonate (K_2CO_3, ≥99.0%), tannic acid (99%), hydrochloric acid (HCl, 37%, CAUTION: corrosive), nitric acid (HNO_3, 70%, CAUTION: corrosive), L-ascorbic acid (≥98%), polyvinylpyrrolidone (PVP, $M_w \approx 55\ 000$ g mol^{-1}), styrene (contains 4-tert-butylcatechol as stabilizer, ≥99%, stored at 4 °C, CAUTION: peroxide former), acrylic acid (contains 180–200 ppm MEHQ inhibitor, 99%, stored at 4 °C), ammonium persulfate (98%), 4-morpholineethanesulfonic acid (MES hydrate buffer, ≥99.5%, stored at 4 °C), N-(3-dimethylaminopropyl)-N′-ethylcarbodiimide hydrochloride (EDAC, BioXtra grade, Sigma Aldrich product code E1769, stored at –20 °C), cysteamine hydrochloride (≥98%, stored at 4 °C), tetraethyl orthosilicate (TEOS, 98%), benzaldehyde (BA, ≥99.5%, purified by redistillation by Sigma-Aldrich, stored in Sure/Seal Sigma-Aldrich bottle in an inert environment), benzyl alcohol (BOH, anhydrous, 99.8%), toluene (TOL, 99.9%), benzoic acid (≥99%), o-xylene (≥99%), and isopropanol (HPLC grade, ≥99.9%) were purchased from Sigma-Aldrich. Absolute ethanol (EtOH) was purchased from KOPTEC. Ultrapure deionised water (Millipore Milli-Q grade, 18.2 MΩ cm^{-1}) was used in all the experiments. All glassware for Au NP synthesis was cleaned with fresh aqua regia (HCl : HNO_3 in 3:1 volume ratio)

overnight, rinsed with excess water, dried at 120 °C, and left to cool to room temperature before use. CAUTION: aqua regia is highly corrosive and should only be handled by trained users under sufficient and appropriate engineering controls and personal protective equipment.

Synthesis of gold nanoparticles. The synthesis of 5 nm Au NPs was adapted from Piella *et al.*,[68] scaled up to produce 600 mL citrate-capped Au NPs (approximately 4.7 nm TEM size, UV-vis absorbance peak at 510 nm) per synthesis – the full procedure is provided in the **Supplementary Methods section of the Supplementary Information**. Ligand exchange was performed by adding 6 mL PVP solution ($M_w \approx 55\,000$ g mol^{-1}, 0.6 g PVP in 6 mL deionised water) to 600 mL Au NP solution and left to stir in air for 1 h. The Au NP solution was stored in the dark until use.

Synthesis of polystyrene colloids. Monodisperse carboxylate-functionalized polystyrene colloidal particles (PS-COOH, *circa* 300 nm in diameter by SEM imaging) were synthesized by the surfactant-free emulsion polymerization of styrene with acrylic acid as a co-monomer and ammonium persulfate as the initiator.[69] 303 mL deionized water (18.2 MΩ cm^{-1}) was added to a three-neck 1 L round bottom flask with a condenser attached. Inert N_2 gas (Airgas, 99.998%, 5 sccm) was bubbled through the reaction mixture for 30 min using a needle placed subsurface while the mixture was heated to 70 °C using a heating mantle under vigorous magnetic stirring (400 rpm). The N_2 needle was then lifted above the stirring solution and positioned above the solution to provide continuous flow of N_2 (3 sccm). 22.5 mL of styrene was added by a glass syringe and the mixture was stirred for 20 min at 70 °C. Acrylic acid solution (150 mg in 1.5 mL deionized water) was then quickly injected into the styrene emulsion. After 5 min of stirring, ammonium persulfate (150 mg in 1.5 mL deionized water) was quickly injected into the emulsion. The emulsion was observed to turn milky white and opaque 30 min after the injection, and the emulsion was left to stir overnight under flowing N_2 (3 sccm). The thus prepared PS-COOH colloids were purified by dialysis over seven days and stored at room temperature until use. The solid content of the PS-COOH suspension was approximately 3–5 wt % (in water) by thermogravimetric analysis (TGA, **Supplementary Fig. 3a**).

Thiol surface functionalization of the purified PS-COOH colloids was performed using a slightly modified previously published procedure.[70] Briefly, 60 mL PS-COOH colloids (5 wt % in water) was centrifuged (12000 G, 40 min) and redispersed in 60 mL MES hydrate buffer (0.25 M) three times. The thus washed PS-COOH colloids in 60 mL MES buffer were transferred into a 500 mL flask. 240 mL of deionized water was then added to the flask and stirred at 500 rpm. While stirring, 12 mL of EDAC solution (2.7 g EDAC dissolved in 12 mL 0.25 M MES hydrate buffer) was added dropwise to the flask over 30 min using a glass dropping funnel. The solution was left to stir for 1 h, after which the mixture in the flask was sonicated at room temperature for 15 min. The flask contents were then centrifuged (12000 G, 30 min) and redispersed in 300 mL deionized water four times before being transferred to a new clean 500 mL flask. While stirring at 500 rpm, 12 mL of cysteamine hydrochloride solution (2.52 g cysteamine hydrochloride, H_2N-C_2H_4-SH, dissolved in 12 mL deionized water) was added dropwise to the flask over 30 min using a glass dropping funnel. The flask was then left to stir overnight in the dark. Following which, the flask contents were centrifuged

(12000 G, 35 min) and redispersed in 300 mL deionized water four times. In the third and fourth redispersion, the pH of the solution mixture was adjusted to pH 4 using 0.1 M HCl. Finally, the thiol-functionalized residue (PS-CONH-C_2H_4-SH) was centrifuged for the fifth time at the same settings, redispersed in 60 mL deionized water, the pH was adjusted to pH 4 using 0.1 M HCl, and the solution was stored at 4 °C until use.

Synthesis of raspberry colloids. Raspberry colloids were prepared by attaching PVP-capped Au NPs to thiol-functionalized polystyrene colloids (PS-CONH-C_2H_4-SH).[49] While continuously stirring 4 mL of PS-CONH-C_2H_4-SH colloids in a 500 mL flask at 600 rpm, 50/100/150/200 mL of PVP-capped Au NP solution (to eventually yield 5/10/15/20PdAu/SiO_2 RCT catalysts) was slowly added dropwise over the course of 1 h. After 1 h, the pH of the pink opaque colloidal mixture was adjusted from neutral to approximately pH 4–5 with 0.7% w/w HNO_3 to facilitate NP attachment to the PS colloids, and the mixture was left to stir for another 15 min. The colloidal mixture was centrifuged (12000 G, 35 min, **Supplementary Fig. 3c**) and redispersed in 50 mL deionized water three times. To the 50 mL of the colloidal dispersion of raspberry colloids in a 500 mL flask, 100 mL of deionized water was added, and the solution pH was adjusted to approximately pH 4–5 with 0.1 M HCl. The low pH slows down unwanted Pd NP nucleation and facilitates selective Pd overgrowth on Au NPs attached to raspberry colloids (**Supplementary Note 8, Supplementary Fig. 18**).[71] While stirring the colloidal dispersion vigorously at 800 rpm, 175/350/525/700 μL of Na_2PdCl_4 solution (10 mM) was quickly added. To prepare the Na_2PdCl_4 solution, solid Na_2PdCl_4 was first dissolved in deionized water, then sonicated for 10 min before passing the solution through a 0.45 μm syringe filter to remove any undissolved solids. Five minutes after the addition of Na_2PdCl_4, 175/350/525/700 μL of L-ascorbic acid solution (40 mM) was quickly added to the flask under vigorous stirring (to eventually yield 5/10/15/20PdAu/SiO_2 RCT catalysts). The flask was wrapped with Al foil to reduce light exposure and left to stir overnight. The originally pink raspberry colloid mixture was observed to turn darker after stirring overnight. Thereafter, the colloidal mixture was centrifuged (12000 G, 35 min) three times, then redispersed in 4 mL deionized water (**Supplementary Fig. 3b**).

RCT catalyst preparation. Raspberry colloid aliquots of 4 mL each were pipetted into separate conical vials to dry in air at 65 °C for 24 h in a convection oven on a vibration-isolation table with the oven fans switched off throughout. This afforded colloidal crystals for further infiltration with a silica precursor. For locally high-metal-density RCT catalysts fabricated by mixing raspberry colloids with bare NP-free PS-CONH-C_2H_4-SH colloids, raspberry colloids that eventually corresponded to 10, 15, or 20 wt % RCT catalysts were mixed with PS-CONH-C_2H_4-SH colloids in a 1:1, 1:2, or 1:3 volume ratio, respectively, while maintaining the same 4 mL total volume in each conical vial.

To each vial with the dried colloidal crystals, 200 μL of pre-hydrolyzed TEOS solution (TEOS : EtOH : 0.1 M HCl = 1:1:1 by volume, stirred for 1 h before use) was added carefully to infiltrate the dried colloidal crystal. Excess TEOS solution was carefully removed using a micropipette. The sample was then placed back in the same oven to dry at 65 °C for 1 h. The process of TEOS infiltration and drying was repeated for a total of three times. To remove the sacrificial PS colloids, the samples were transferred from the conical vial to a 7 dram glass vial

and calcined in static air (ramp temperature from room temperature to 500 °C over 5 h, hold at 500 °C for 2 h, then left to cool to room temperature over 3–4 h) to yield the RCT catalyst. Approximately 40–50 mg of RCT catalysts were produced for every 4 mL raspberry colloid aliquot. For catalysis testing, TEM imaging and tomography, ICP-MS analysis, XRD analysis, and CO chemisorption analysis, RCT catalysts were first crushed and sieved to 106–300 μm.

Electron microscopy, energy dispersive X-ray spectroscopy (EDX). Scanning electron microscopy (SEM) images were acquired in the secondary electron and backscattered electron mode using GeminiSEM 560 (Zeiss) at an accelerating voltage of 2.5 keV and working distance of 5 nm. To prepare TEM grids for TEM, STEM, and EDX, samples were dispersed in absolute ethanol and drop-casted onto a Formvar/Carbon 200 mesh copper grid (Ted Pella). Bright-field transmission electron microscopy (BF-TEM) imaging, high-angle annular dark field scanning transmission electron microscopy (HAADF STEM), and energy-dispersive X-ray spectroscopy (EDX) were performed using a JEOL ARM 200F STEM equipped with a cold field emission gun (200 keV) and integrated aberration corrector (Cs). STEM-EDX was done using Octane 100 mm^2 detector (EDAX Metek), and the data analyzed using the TEAM software. NP size distribution was determined by measuring the diameters of approximately 200–300 NPs (per catalyst) from their BF-TEM images in the ImageJ software.

Electron tomography. Two single axis HAADF-STEM tomography tilt series were recorded on a FEI Talos F200X operated at 200 kV. A high tilt tomography holder (Fischione, FP90997/19 tomography holder) was used. Fiducial markers (10 nm Au NPs) were drop casted on a Formvar/Carbon 200 mesh copper grid (Ted Pella) prior to drop casting 30 μL of the 5/20PdAu/SiO_2 RCT catalysts dispersed in absolute ethanol. Each tilt series consisted of 71 images from –70 ° to +70° at a step size of 2° and were acquired using the Tomography STEM software version 4.15 from FEI (Thermo Fisher Scientific). Between each image acquisition, the beam was blanked to avoid beam damage. The acquisition was performed with spot size 9, camera length of 160 mm, collection angle of 35–200 mrad, extraction voltage of 4150 V, and probe current of 0.014 nA. The images were acquired with 2048 × 2048 pixels with a size of 728.5 pm, a dwell time of 1 μs per pixel and a total frame time of 8.08 s. The reconstruction was performed with the IMOD software.[72] The coarse and fine alignment of the tilt series were performed *via* cross-correlation and manual tracking of the Au NP fiducial markers, respectively. The tilt series were binned by a factor of two and reconstructed using a weighted back-projection algorithm. Detailed analysis of the reconstructed electron tomograms to obtain the average center-to-center interparticle distance is provided in **Supplementary Note 1**.[73,74]

UV-vis and infrared spectroscopy, thermogravimetric analysis (TGA), zeta potential measurements, inductively coupled plasma-mass spectrometry (ICP-MS), X-ray photoelectron spectroscopy (XPS), CO chemisorption analysis, powder X-ray diffraction (XRD). Details are provided in the **Supplementary Methods section of the Supplementary Information**.

Catalytic testing. Liquid phase benzaldehyde hydrogenation was conducted in a 50 mL stainless steel autoclave batch reactor (Parr 5512 Compact Bench Top Reactor equipped with Parr 4848 Reaction Controller). In a typical reaction, benzaldehyde (162.6 μL, 50 mM, purified by redistillation by Sigma-Aldrich, stored in Sure/Seal Sigma-Aldrich bottle in an inert environment) and o-xylene (internal standard, 77.3 μL, 20 mM) were dissolved in 31.76 mL of

HPLC-grade isopropanol solvent and mixed thoroughly to form a final volume of 32 mL. Given that BA was known to auto-oxidize in air to benzoic acid,[75] an initial aliquot of 1.5 mL was withdrawn to check for the purity of the solution mixture using GC-MS analysis before the start of every reaction. Benzoic acid was not detected by GC-MS analysis in the BA reagent in the initial aliquot or at any point during the reaction and was not expected to affect BA hydrogenation even if present in trace quantities (**Supplementary Fig. 19**).

Thereafter, 3–15 mg of sieved catalyst ($m_{cat,}$ sieved to 106–300 μm) was added to the remaining 30.5 mL of solution mixture. When the metal mass (m_{metal}) is fixed at 0.6 mg, the BA reactant : Pd active site ratio is ≈ 4300. m_{metal} is given by the product of m_{cat} and metal loading. The reactor was then assembled, vigorous stirring (1000 rpm) engaged to eliminate external diffusional limitations, and the reactor purged four times with N_2 gas (Airgas, 99.998%, approximately 30 bar) to remove air from the reactor. The reactor was pressurized three times with H_2 gas (Airgas, 99.999%, 20 bar) to saturate the reaction solution with H_2, then the reactor was heated to the reaction temperature of 150 °C and reaction time set to $t = 0$. Once the set reactor temperature was reached and stable (typically taking 15 min), the heated reactor was depressurized to 20 bar H_2. The batch reactor was left to react for 24 h and sample aliquots of approximately 0.2 mL each were withdrawn at specific time intervals from the reactor's liquid sampling valve dip tube into 1.5 mL autosampler glass vials lined with 0.2 mL glass insets to minimize headspace volume. After each sampling, the reactor was repressurized back to 20 bar H_2. The concentration of BA, BOH, and TOL in the sample aliquot was quantified by *ex situ* gas chromatography-mass spectrometry (GC-MS) analysis using Agilent 7890A GC (HP-1MS column, 30 m length, 0.25 mm diameter, 0.25 μm film thickness, Agilent part number 19091S-933), Agilent 5975C MS, and Agilent 7693 autosampler. Trace quantities of the acetal adduct from benzaldehyde reaction with isopropanol solvent was detected (< 0.2% selectivity by GC-MS analysis). The acetal adduct was not expected to contribute to TOL formation, as previous kinetic modeling reported that the rate of acetal to ether and ether to TOL formation was 24 and 2400 times slower than BA to BOH conversion, respectively.[43] For quantification, a calibration curve was prepared with o-xylene as the internal standard.[40]

For liquid phase benzyl alcohol hydrogenation, benzyl alcohol at the same concentration (50 mM) was used instead of benzaldehyde. To determine the apparent activation energy, liquid phase benzaldehyde hydrogenation was carried out at 130, 140, and 160 °C while maintaining the same pressure (20 bar H_2). The reaction order of benzaldehyde was determined by varying its initial concentration (30, 40, 60 mM) while keeping the same H_2 pressure (20 bar) and reaction temperature (150 °C). The reaction order of H_2 was determined by varying its pressure (15, 17.5, 22.5 bar) while keeping the same benzaldehyde concentration (50 mM) and reaction temperature (150 °C).

Calculation methods for catalytic descriptors (benzaldehyde conversion, product selectivity, benzyl alcohol yield, 1st order rate constant, turnover frequency) are provided in the **Supplementary Methods section of the Supplementary Information**.

Interparticle distance modeling. The average center-to-center interparticle distance at various metal loadings was modeled using a 2D geometric model[46] and 2D Poisson statistical model.[47] Full model details are provided in **Supplementary Note 2**.

COMSOL concentration profile modeling and simulations. 2D diffusion transport modeling was implemented in COMSOL Multiphysics 5.6 to solve equations (1) and (2) under various interparticle distance conditions using our model shown in **Supplementary Fig. 13a**). We opted for a continuous fluid model as (1) the internal diffusion regime is non-Knudsen (**Supplementary Note 6**), (2) the number of molecules involved to accurately describe the catalytic system overwhelms discrete molecular dynamics simulations (the BOH generation rate is 7×10^{-5} mol m^{-2} s^{-1} per NP in a solvent of pure isopropanol, which must also be included in the simulations), and (3) COMSOL simulations based on a continuous fluid model have been adopted for similar applications in prior literature.[21,22] In (1) and (2), c refers to the concentration of BOH, D is the diffusion coefficient of BOH, R is the BOH production rate, and N is the BOH flux. **Supplementary Table 6** shows a list of modeling parameters with their associated values. The BOH production rate, R, is extracted from TOF values obtained at t = 0.5 h in catalytic tests using 12 mg of RCT catalysts (**Fig. 3d**).

$$\frac{\partial c}{\partial t} + \nabla(-D\,\nabla c) = R \quad (1)$$

$$N = -D\,\nabla c \quad (2)$$

DATA AVAILABILITY

Data that support the findings of this study are available within the paper, Supplementary Information, and Source Data files. Additional data is available from the authors upon reasonable request.

ACKNOWLEDGEMENTS

This work was supported by the Integrated Mesoscale Architectures for Sustainable Catalysis (IMASC), an Energy Frontier Research Center funded by the U.S. Department of Energy, Office of Science, Basic Energy Sciences under Award Number DE-SC0012573 (S.K.K., J.A.), by the U. S. Defense Threat Reduction Agency (DTRA) under Award Number HDTR1211001612 (K.R.G.L., H.W., S.G., M.A.), and by the Starting PI Fund of the Electron Microscopy Center at Utrecht University (M.P.P., J.E.S.v.d.H.). Electron microscopy, thermogravimetric analysis, zeta potential measurements, infrared spectroscopy, X-ray photoelectron spectroscopy, and CO chemisorption measurements were performed at the Center for Nanoscale Systems (CNS), a member of the National Nanotechnology Coordinated Infrastructure Network (NNCI), which is supported by the National Science Foundation under NSF ECCS Award Number 1541959. K.R.G.L., M.A., and J.A. thank Prof. Cynthia Friend for the use of her laboratory facilities to conduct the batch hydrogenation catalytic reactions. K.R.G.L. acknowledges financial support from the Agency for Science, Technology and Research (A*STAR) Singapore National Science Scholarship (PhD). S.K.K. acknowledges the Swiss National Science Foundation for the award of an Early Postdoc. Mobility fellowship (SNSF Grant Number P2EZP2_199972). K.R.G.L. thanks Prof. Robert J. Madix, Dr. Jules Gardener, Dr. Shucong Li, Mr. H. Greg. Lin, and Dr. Julian Hungerford for the helpful discussions on the analysis of catalytic, STEM-EDX, small-angle X-ray scattering, XPS, and CO chemisorption data, respectively.

AUTHOR CONTRIBUTIONS

K.R.G.L. and S.K.K. contributed equally to this work. K.R.G.L. conceived the research idea and coordinated the work. K.R.G.L., S.K.K., M.A., and J.A. designed the experiments. K.R.G.L., supported by S.G., synthesized, characterized, and analyzed the materials. K.R.G.L., guided by S.K.K., conducted catalysis testing, kinetic modeling, and analyzed the results. M.P.P., supervised by J.E.S.v.d.H., performed the electron tomography experiments and analyzed the data. K.R.G.L., S.G., and M.P.P. calculated the interparticle distances. H.W. performed the COMSOL modeling. H.W. and K.R.G.L. analyzed the COMSOL modeling results. K.R.G.L. and S.K.K. wrote the manuscript with input from all the authors. J.A. supervised the entire work. All authors have given approval to the final version of the manuscript.

COMPETING INTERESTS

The authors declare no competing interests.

ADDITIONAL INFORMATION

Supplementary Information. Supplementary Methods, Supplementary Note 1–8, Supplementary Fig. 1–19, Supplementary Table 1–6, Supplementary Video 1–4, and Supplementary References are available online in the Supplementary Information.

Correspondence and requests for materials should be addressed to jaiz@seas.harvard.edu (J. A.).

REFERENCES

1. Rothenberg, G. *Catalysis: concepts and green applications*. (Wiley-VCH, 2008).
2. Friend, C. M. & Xu, B. Heterogeneous Catalysis: A Central Science for a Sustainable Future. *Acc. Chem. Res.* **50**, 517–521 (2017).
3. Munnik, P., de Jongh, P. E. & de Jong, K. P. Recent Developments in the Synthesis of Supported Catalysts. *Chem. Rev.* **115**, 6687–6718 (2015).
4. van Deelen, T. W., Hernández Mejía, C. & de Jong, K. P. Control of metal-support interactions in heterogeneous catalysts to enhance activity and selectivity. *Nat. Catal.* **2**, 955–970 (2019).
5. Shi, Y. *et al.* Noble-Metal Nanocrystals with Controlled Shapes for Catalytic and Electrocatalytic Applications. *Chem. Rev.* **121**, 649–735 (2021).
6. Liu, L. & Corma, A. Metal Catalysts for Heterogeneous Catalysis: From Single Atoms to Nanoclusters and Nanoparticles. *Chem. Rev.* **118**, 4981–5079 (2018).
7. Wang, Y. *et al.* Recent advances in ordered meso/macroporous metal oxides for heterogeneous catalysis: a review. *J. Mater. Chem. A* **5**, 8825–8846 (2017).
8. Yamada, Y. *et al.* Nanocrystal bilayer for tandem catalysis. *Nat. Chem.* **3**, 372–376 (2011).
9. Holm, A. *et al.* Nanoscale Spatial Distribution of Supported Nanoparticles Controls Activity and Stability in Powder Catalysts for CO Oxidation and Photocatalytic H_2 Evolution. *J. Am. Chem. Soc.* **142**, 14481–14494 (2020).
10. Elias, R. C. & Linic, S. Elucidating the Roles of Local and Nonlocal Rate Enhancement Mechanisms in Plasmonic Catalysis. *J. Am. Chem. Soc.* **144**, 19990–19998 (2022).

11. Keijzer, P. H., van den Reijen, J. E., Keijzer, C. J., de Jong, K. P. & de Jongh, P. E. Influence of atmosphere, interparticle distance and support on the stability of silver on α-alumina for ethylene epoxidation. *J. Catal.* **405**, 534–544 (2022).
12. Goodman, E. D. *et al.* Size-controlled nanocrystals reveal spatial dependence and severity of nanoparticle coalescence and Ostwald ripening in sintering phenomena. *Nanoscale* **13**, 930–938 (2021).
13. Yin, P. *et al.* Quantification of critical particle distance for mitigating catalyst sintering. *Nat. Commun.* **12**, 4865 (2021).
14. Goodman, E. D. *et al.* Catalyst deactivation via decomposition into single atoms and the role of metal loading. *Nat. Catal.* **2**, 748–755 (2019).
15. Aitbekova, A. *et al.* Templated encapsulation of platinum-based catalysts promotes high-temperature stability to 1,100 °C. *Nat. Mater.* **21**, 1290–1297 (2022).
16. Prieto, G., Zečević, J., Friedrich, H., de Jong, K. P. & de Jongh, P. E. Towards stable catalysts by controlling collective properties of supported metal nanoparticles. *Nat. Mater.* **12**, 34–39 (2013).
17. Kumar, S. & Zou, S. Electrooxidation of CO on Uniform Arrays of Au Nanoparticles: Effects of Particle Size and Interparticle Spacing. *Langmuir* **25**, 574–581 (2009).
18. Inaba, M. *et al.* The Oxygen Reduction Reaction on Pt: Why Particle Size and Interparticle Distance Matter. *ACS Catal.* **11**, 7144–7153 (2021).
19. Nesselberger, M. *et al.* The effect of particle proximity on the oxygen reduction rate of size-selected platinum clusters. *Nat. Mater.* **12**, 919–924 (2013).
20. Fortunato, G. V. *et al.* Impact of Palladium Loading and Interparticle Distance on the Selectivity for the Oxygen Reduction Reaction toward Hydrogen Peroxide. *J. Phys. Chem. C* **122**, 15878–15885 (2018).
21. Lum, Y. & Ager, J. W. Sequential catalysis controls selectivity in electrochemical CO_2 reduction on Cu. *Energy Environ. Sci.* **11**, 2935–2944 (2018).
22. Mistry, H. *et al.* Tuning Catalytic Selectivity at the Mesoscale via Interparticle Interactions. *ACS Catal.* **6**, 1075–1080 (2016).
23. Zecevic, J., Vanbutsele, G., de Jong, K. P. & Martens, J. A. Nanoscale intimacy in bifunctional catalysts for selective conversion of hydrocarbons. *Nature* **528**, 245–248 (2015).
24. Karim, W. *et al.* Catalyst support effects on hydrogen spillover. *Nature* **541**, 68–71 (2017).
25. Dai, J. & Zhang, H. Recent Advances in Catalytic Confinement Effect within Micro/Meso-Porous Crystalline Materials. *Small* **17**, 2005334 (2021).
26. Le, T. T. *et al.* Elemental zoning enhances mass transport in zeolite catalysts for methanol to hydrocarbons. *Nat. Catal.* **6**, 254–265 (2023).
27. Liu, J. *et al.* MOF-enabled confinement and related effects for chemical catalyst presentation and utilization. *Chem. Soc. Rev.* **51**, 1045–1097 (2022).
28. Zhang, J., Wang, B., Nikolla, E. & Medlin, J. W. Directing Reaction Pathways through Controlled Reactant Binding at Pd–TiO_2 Interfaces. *Angew. Chem. Int. Ed.* **56**, 6594–6598 (2017).
29. Durndell, L. J. *et al.* Selectivity control in Pt-catalyzed cinnamaldehyde hydrogenation. *Sci. Rep.* **5**, 9425 (2015).
30. Parlett, C. M. A., Bruce, D. W., Hondow, N. S., Lee, A. F. & Wilson, K. Support-Enhanced Selective Aerobic Alcohol Oxidation over Pd/Mesoporous Silicas. *ACS Catal.* **1**, 636–640 (2011).
31. Cargnello, M. Colloidal Nanocrystals as Building Blocks for Well-Defined Heterogeneous Catalysts. *Chem. Mater.* **31**, 576–596 (2019).
32. Losch, P. *et al.* Colloidal nanocrystals for heterogeneous catalysis. *Nano Today* **24**, 15–47 (2019).

33. Cargnello, M. *et al.* Efficient Removal of Organic Ligands from Supported Nanocrystals by Fast Thermal Annealing Enables Catalytic Studies on Well-Defined Active Phases. *J. Am. Chem. Soc.* **137**, 6906–6911 (2015).
34. Lu, L., Zou, S. & Fang, B. The Critical Impacts of Ligands on Heterogeneous Nanocatalysis: A Review. *ACS Catal.* **11**, 6020–6058 (2021).
35. Collins, G., Davitt, F., O'Dwyer, C. & Holmes, J. D. Comparing Thermal and Chemical Removal of Nanoparticle Stabilizing Ligands: Effect on Catalytic Activity and Stability. *ACS Appl. Nano Mater.* **1**, 7129–7138 (2018).
36. Eppler, A. S., Rupprechter, G., Guczi, L. & Somorjai, G. A. Model Catalysts Fabricated Using Electron Beam Lithography and Pulsed Laser Deposition. *J. Phys. Chem. B* **101**, 9973–9977 (1997).
37. Shirman, E. *et al.* Modular Design of Advanced Catalytic Materials Using Hybrid Organic-Inorganic Raspberry Particles. *Adv. Funct. Mater.* **28**, 1704559 (2018).
38. Singh, N. *et al.* Aqueous phase catalytic and electrocatalytic hydrogenation of phenol and benzaldehyde over platinum group metals. *J. Catal.* **382**, 372–384 (2020).
39. Bhanushali, J. T., Kainthla, I., Keri, R. S. & Nagaraja, B. M. Catalytic Hydrogenation of Benzaldehyde for Selective Synthesis of Benzyl Alcohol: A Review. *ChemistrySelect* **1**, 3839–3853 (2016).
40. Kaiser, S. K. *et al.* Identifying the Optimal Pd Ensemble Size in Dilute PdAu Alloy Nanomaterials for Benzaldehyde Hydrogenation. *ACS Catal.* **13**, 12092–12103 (2023).
41. Song, Y. *et al.* Hydrogenation of benzaldehyde via electrocatalysis and thermal catalysis on carbon-supported metals. *J. Catal.* **359**, 68–75 (2018).
42. Cheng, G. *et al.* Critical role of solvent-modulated hydrogen-binding strength in the catalytic hydrogenation of benzaldehyde on palladium. *Nat. Catal.* **4**, 976–985 (2021).
43. Procházková, D., Zámostný, P., Bejblová, M., Červený, L. & Čejka, J. Hydrodeoxygenation of aldehydes catalyzed by supported palladium catalysts. *Appl. Catal. A: Gen.* **332**, 56–64 (2007).
44. Hoeven, J. E. S. *et al.* On the Origin of Sinter-Resistance and Catalyst Accessibility in Raspberry-Colloid-Templated Catalyst Design. *Adv. Funct. Mater.* **31**, 2106876 (2021).
45. Batista, A. T. F. *et al.* Atomic Scale Insight into the Formation, Size, and Location of Platinum Nanoparticles Supported on γ-Alumina. *ACS Catal.* **10**, 4193–4204 (2020).
46. Meier, J. C. *et al.* Design criteria for stable Pt/C fuel cell catalysts. *Beilstein J. Nanotechnol.* **5**, 44–67 (2014).
47. Tournus, F. Random nanoparticle deposition: inter-particle distances in 2D, 3D, and multilayer samples. *J. Nanopart. Res.* **13**, 5211–5223 (2011).
48. Okamoto, M., Hirao, T. & Yamaai, T. Polymers as novel modifiers for supported metal catalyst in hydrogenation of benzaldehydes. *J. Catal.* **276**, 423–428 (2010).
49. van der Hoeven, J. E. S. *et al.* Entropic Control of HD Exchange Rates over Dilute Pd-in-Au Alloy Nanoparticle Catalysts. *ACS Catal.* **11**, 6971–6981 (2021).
50. Luneau, M. *et al.* Achieving High Selectivity for Alkyne Hydrogenation at High Conversions with Compositionally Optimized PdAu Nanoparticle Catalysts in Raspberry Colloid-Templated SiO_2. *ACS Catal.* **10**, 441–450 (2020).
51. Hao, Y., Pischetola, C., Cárdenas-Lizana, F. & Keane, M. A. Selective Liquid Phase Hydrogenation of Benzaldehyde to Benzyl Alcohol Over Alumina Supported Gold. *Catal. Lett.* **150**, 881–887 (2020).
52. Mohamed-Ibrahim, N. A. binte *et al.* Applying Magnetic-Responsive Nanocatalyst-Liquid Interface for Active Molecule Manipulation to Boost Catalysis Beyond Diffusion Limit. *ChemCatChem* **14**, (2022).
53. Cui, T. *et al.* Encapsulating Palladium Nanoparticles Inside Mesoporous MFI Zeolite Nanocrystals for Shape-Selective Catalysis. *Angew. Chem. Int. Ed.* **55**, 9178–9182 (2016).

54. Shirman, E., Shirman, T., Aizenberg, M. & Aizenberg, J. Enhanced catalytic materials with partially embedded catalytic nanoparticles. U.S. patent 11,590,483 B2 (2023).
55. Kolle, M., Shirman, T., Aizenberg, M., Vogel, N. & Aizenberg, J. High-surface area functional material coated structures. U.S. patent 11,325,114 B2 (2022).
56. Kao, K. *et al.* A General Approach for Monolayer Adsorption of High Weight Loadings of Uniform Nanocrystals on Oxide Supports. *Angew. Chem. Int. Ed.* **60**, 7971–7979 (2021).
57. Casavola, M., Hermannsdörfer, J., De Jonge, N., Dugulan, A. I. & De Jong, K. P. Fabrication of Fischer-Tropsch Catalysts by Deposition of Iron Nanocrystals on Carbon Nanotubes. *Adv. Funct. Mater.* **25**, 5309–5319 (2015).
58. Santos, H. & Costa, M. Analysis of the mass transfer controlled regime in automotive catalytic converters. *Int. J. Heat Mass Transf.* **51**, 41–51 (2008).
59. Lohr, T. L. & Marks, T. J. Orthogonal tandem catalysis. *Nat. Chem.* **7**, 477–482 (2015).
60. Climent, M. J., Corma, A., Iborra, S. & Sabater, M. J. Heterogeneous Catalysis for Tandem Reactions. *ACS Catal.* **4**, 870–891 (2014).
61. Isaacs, M. A. *et al.* A spatially orthogonal hierarchically porous acid–base catalyst for cascade and antagonistic reactions. *Nat. Catal.* **3**, 921–931 (2020).
62. Wheeldon, I. *et al.* Substrate channelling as an approach to cascade reactions. *Nat. Chem.* **8**, 299–309 (2016).
63. Zou, H. *et al.* Dual metal nanoparticles within multicompartmentalized mesoporous organosilicas for efficient sequential hydrogenation. *Nat. Commun.* **12**, 4968 (2021).
64. Zou, N. *et al.* Cooperative communication within and between single nanocatalysts. *Nat. Chem.* **10**, 607–614 (2018).
65. Cheng, K. *et al.* Maximizing noble metal utilization in solid catalysts by control of nanoparticle location. *Science* **377**, 204–208 (2022).
66. Xiao, J. *et al.* Tandem catalysis with double-shelled hollow spheres. *Nat. Mater.* **21**, 572–579 (2022).
67. Parlett, C. M. A. *et al.* Spatially orthogonal chemical functionalization of a hierarchical pore network for catalytic cascade reactions. *Nat. Mater.* **15**, 178–182 (2016).
68. Piella, J., Bastús, N. G. & Puntes, V. Size-Controlled Synthesis of Sub-10-nanometer Citrate-Stabilized Gold Nanoparticles and Related Optical Properties. *Chem. Mater.* **28**, 1066–1075 (2016).
69. Vogel, N., de Viguerie, L., Jonas, U., Weiss, C. K. & Landfester, K. Wafer-Scale Fabrication of Ordered Binary Colloidal Monolayers with Adjustable Stoichiometries. *Adv. Funct. Mater.* **21**, 3064–3073 (2011).
70. Shi, W., Sahoo, Y., Swihart, M. T. & Prasad, P. N. Gold Nanoshells on Polystyrene Cores for Control of Surface Plasmon Resonance. *Langmuir* **21**, 1610–1617 (2005).
71. van der Hoeven, J. E. S. *et al.* Structural Control over Bimetallic Core–Shell Nanorods for Surface-Enhanced Raman Spectroscopy. *ACS Omega* **6**, 7034–7046 (2021).
72. Kremer, J. R., Mastronarde, D. N. & McIntosh, J. R. Computer Visualization of Three-Dimensional Image Data Using IMOD. *J. Struct. Biol.* **116**, 71–76 (1996).
73. Bolte, S. & Cordelières, F. P. A guided tour into subcellular colocalization analysis in light microscopy. *J. Microsc.* **224**, 213–232 (2006).
74. Schindelin, J. *et al.* Fiji: an open-source platform for biological-image analysis. *Nat. Methods* **9**, 676–682 (2012).
75. Sankar, M. *et al.* The benzaldehyde oxidation paradox explained by the interception of peroxy radical by benzyl alcohol. *Nat. Commun.* **5**, 3332 (2014).